





Cite this: *RSC Adv.*, 2022, 12, 3721

# Calcium vapor synthesis of extremely coercive $\text{SmCo}_5$ †

Sarah E. Baker, Alexander A. Baker, \* Christine A. Orme, Matthew A. Worthington, Tian T. Li,  Edwin M. Sedillo, Jessica Dudoff, Jonathan R. I. Lee, Joshua D. Kuntz and Scott K. McCall \*

Exceptionally coercive  $\text{SmCo}_5$  particles are produced through calcium vapor reduction of  $\text{SmCo}_5\text{O}_9$  powders synthesized by flame spray pyrolysis. The resulting powders are composed of oblate hexagonal particles approximately 2 microns across with smooth surfaces. This microstructure yields record-breaking room temperature coercivity  $H_{c,i} > 80$  kOe, or  $> 60$  kOe when combined with advanced manufacturing approaches such as electrophoretic deposition or molding with tetraglyme inks. These techniques enable straightforward low-loss fabrication of bulk parts. The high coercivity is extremely robust at elevated temperatures, exceeding 10 kOe even at 600 °C. The oxide precursor approach removes the need for strict environmental control during synthesis that is common to other nanoparticle-based routes and can readily be scaled to kilogram quantities of feedstock production. Magnet powders produced by calcium vapor reduction can thus function as the building blocks for traditional or advanced manufacturing techniques, while the high coercivity enables consistent performance across a wide range of temperatures.

Received 28th September 2021

Accepted 19th January 2022

DOI: 10.1039/d1ra07244g

rsc.li/rsc-advances

High-performance rare earth permanent magnets (REPMs) are integral to modern technology, from small actuators in ear buds, to compact motor-generators in electric vehicles.<sup>1,2</sup> Even modest gains in magnet performance or design optimization have great impact on energy consumption.<sup>3</sup> While most magnet production proceeds through synthesis and powder production followed by pressing, sintering, and grinding to achieve the desired shape,<sup>4,5</sup> an attractive alternative is the controlled synthesis of high performance nanostructured materials, which can then be assembled using bottom-up fabrication approaches. Applying this philosophy to Sm-Co, excellent magnetic properties can be obtained by controlled reduction of oxide precursors, through the use of reducing agents such as KCl or Ca.<sup>6–9</sup> However, most studies have been limited to small batches, and have stringent synthesis requirements to achieve optimal properties. Here,  $\text{SmCo}_5\text{O}_9$  powders produced in gram to kilogram quantities by flame-spray pyrolysis can be reduced in the presence of Ca vapor to form micron-scale particles with coercivity in excess of 80 kOe. Further, the oxide powders are amenable to advanced manufacturing techniques such as electrophoretic deposition or molding, an important step towards net-shape fabrication of high temperature permanent magnets.

When designing a material for real applications production cost and machinability must be considered. As with many functional materials, REPMs are brittle and prone to fracture, inflating production costs due to part breakage and swarfs, which often exceed 25% of the starting material, and can be over 50% for small parts or prototypes.<sup>10</sup> Advanced manufacturing fabrication routes using nanostructured powder feedstocks in combination with techniques such as: 3D printing<sup>11–13</sup> and laser additive,<sup>14,15</sup> are promising alternatives for production of net-shape parts. However, melting magnetic powders typically destroys the coercivity earned from micro-structure engineering.<sup>16</sup>

Magnet optimization often focuses on enhancing the coercivity,  $H_c$ , by controlling grain size, orientation, and grain boundary phases,<sup>3,17</sup> but must also maintain high remnant magnetization,  $M_r$ . The ideal magnet is composed of aligned, highly coercive, non-interacting grains.<sup>3</sup> Control of coercivity in powders and sintered magnets is typically achieved through tailoring of the synthesis route to produce grain boundary phases that isolate grains without locally reducing magnetic anisotropy.<sup>17,18</sup> Domain wall motion and growth of reverse domains is inhibited by isolating each grain from its neighbors, preventing a single reversal event from cascading across the entire structure, and by the presence of defects or inclusions that can act as pinning sites.<sup>19</sup> A limitation of this approach is that the anisotropy field is locally reduced around such sites, thereby promoting the nucleation of reverse domains.<sup>3</sup> Similar challenges arise when the particles have irregular shapes, as

Lawrence Livermore National Laboratory, Livermore, CA, 94550, USA. E-mail: baker97@llnl.gov; mccall10@llnl.gov

† Electronic supplementary information (ESI) available. See DOI: 10.1039/d1ra07244g



locally enhanced demagnetization fields provide nucleation centers for reversal.<sup>20</sup> Magnets can be classified according to whether their coercivity is limited by nucleation of reverse domains or motion of domain walls, though in practice both must be considered.<sup>21</sup> Top-down approaches to the fabrication of magnetic powders, such as ball- or jet-milling, offer little control of these factors, necessitating the development of techniques such as grain-boundary diffusion<sup>22–25</sup> and grain refinement<sup>26</sup> to enhance coercivity. Bottom-up approaches, in contrast, offer far greater control of local composition, microstructure, and size distribution, albeit typically at the cost of significantly smaller production volumes.<sup>9</sup> By minimizing the presence of microstructural defects within grains and avoiding secondary phase formation, it is possible to produce a magnetic powder significantly more resistant to the nucleation of reverse magnetic domains.

Extensive work developing precursor powders has created nanoparticles suitable for assembly into a bulk nanostructured magnet. Surfactant assisted ball milling can reduce bulk Sm–Co to nanosized particles with moderate coercivities, but provides only limited control over size or shape.<sup>23–25,27</sup> Direct solution phase synthesis of reduced SmCo<sub>5</sub> nanoparticles from metal salts is challenging due to the extremely negative reduction potentials of Sm<sup>2+</sup> (−2.3 eV) and Sm<sup>3+</sup> (−2.68 eV), which causes rapid re-oxidation of metallic Sm nanoparticles even under a controlled atmosphere.<sup>28</sup> Reduction of oxide precursors using KCl or Ca along with graphene to inhibit particle growth,<sup>7</sup> or SmCo–O pods<sup>9</sup> combined with Ca, CaO, and KCl has led to nanoparticles with  $H_{c,i} = 24$  kOe and 50 kOe, respectively. This latter value is the highest coercivity achieved to date for ferromagnetic nanoparticles. Despite these advances, challenges remain for the scaling of these techniques, due to the stringent atmospheric control requirements.

Herein, a scalable process for fabrication of SmCo<sub>5</sub> magnet feedstocks with extremely high coercivities is demonstrated for use with AM techniques including electrophoretic deposition, ink-based molding, or extrusion. The process begins with flame spray pyrolysis of Sm–Co–O nanoparticles capable of producing feedstocks with both tunable stoichiometry and particle sizes at production rates of kgs per hour and suitable for expansion to large-volume industrial applications. Solution phase suspensions of these non-magnetic particles enable assembly without the challenges of agglomeration associated with ferromagnetic particles. Subsequently, the greenbodies are converted to sintered magnets *via* calciothermic reduction. In contrast to previous approaches, the samples are not directly mixed with the reducing agent, instead being placed above a bath such that vapor penetrates the sample greenbody to form SmCo<sub>5</sub>. The magnets produced consistently display room temperature coercivities up to 80 kOe (the highest ever reported for a permanent magnet) in powder form, and above 60 kOe in bulk. High-temperature measurements show they retain  $H_{c,i} = 10$  kOe even at 600 °C. These properties are attributed to the particle size and morphology inhibiting the formation of multiple domains in a single particle, and the absence of defects preventing the nucleation of reverse domains. The

isotropic structure of the grains leads to  $M_s \sim 7$  kG and  $M_r \sim 5$  kG.

Sm–Co–O particles 30–100 nm in diameter (Fig. 1a) were produced from oxide precursors. After heat treatment at 875 °C in the presence of Ca vapor the particles ripen to oblate hexagons consistent with the SmCo<sub>5</sub> habit, typically 1.0 μm along the short axis and 1.8 μm in the long axis (Fig. 1b), and sinter together to form a porous structure approximately 60% dense. Histograms of particle size for representative samples are shown in Fig. 1c and d. Particle growth is limited by the presence of CaO, which forms through reaction between Ca vapor and the Sm–Co–O precursor (and which reacts to form CaCO<sub>3</sub> upon removal from the controlled atmosphere of the furnace) and can be removed by washing in degassed water. Alternatively, the Sm–Co–O nanoparticles can be dispersed in ethanol and assembled into arbitrary shapes directed by electrophoretic deposition (EPD). A schematic of the EPD deposition chamber and the resulting greenbodies are shown in Fig. 1e and f. Such greenbodies are brittle until subjected to the calciothermic reduction treatment, whereupon they contract and sinter to

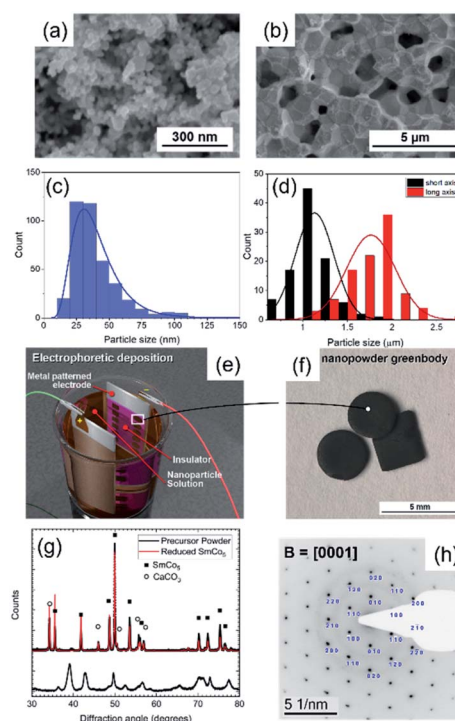


Fig. 1 (a) SmCoO precursor powder, composed of sub-100 nm particles, and (b) the hexagonal grains of SmCo<sub>5</sub> formed after calciothermic reduction treatment, after washing in degassed water. Histograms of particle size for the precursor and reduced powder are shown in (c) and (d), respectively, along with fits to the distributions. A schematic of the EPD deposition chamber is shown in (e), indicating an option for advanced manufacturing using these powders, and in (f) representative greenbodies produced by this technique. XRD (g) confirms the formation of SmCo<sub>5</sub> (dots are data points, solid line is a fit conducted with GSAS-II), with an excess CaCO<sub>3</sub> phase that can be removed by washing the sample in degassed water. TEM electron diffraction across one of the grains from (b), shown in (h), shows well defined spots from an oriented crystal.



form mechanically robust parts. Similarly, the nanoparticles can be mixed with a shear-thinning ink and pressed into molds or extruded; once the ink has been evaporated by overnight baking at 60 °C the same calciothermic treatment is performed. Directing the assembly of oxide particles allows handling of particles that are neither air sensitive nor magnetic, allowing facile and reproducible particle dispersion in suspension, which is essential for both EPD<sup>29</sup> and molding. In the case of these bulk parts the annealing step must be lengthened from 1 to 12 hours to allow the Ca vapor to penetrate through the material and fully convert the Sm–Co–O to SmCo<sub>5</sub>. XRD patterns taken before and after the reduction process (Fig. 1g) show the formation of SmCo<sub>5</sub>, without secondary Sm<sub>2</sub>Co<sub>17</sub> or Sm<sub>2</sub>Co<sub>7</sub> phases, along with CaCO<sub>3</sub> (likely formed from reaction of CaO from the reduction with CO<sub>2</sub> in the air). Rietveld refinement was performed using GSAS-II to confirm phase purity,<sup>30</sup> additional phases did not improve fit quality. The crystallite size determined through this process was 625 nm, suggesting each particle is composed of 2–4 crystallites. Such grain boundaries are not visible in TEM measurements (Fig. 2a), and electron diffraction patterns taken across the extend of a single particle (Fig. 1h) suggested particles did not show a smearing of the spot pattern.

The grain morphology for a molded sample is presented in Fig. 2a, and reveals smooth surfaces without jagged edges or points, thereby limiting nucleation sites for reversal of the magnetic domains. Cross-sectional SEM measurements of the

microstructure of a molded sample (Fig. 2b) reveals a porous network of interconnected grains. Extensive work on Nd<sub>2</sub>Fe<sub>14</sub>B magnets has shown that the introduction of a grain boundary phase that isolates the grains is crucial to achieving the highest coercivities,<sup>31</sup> with processes such as liquid phase sintering improving magnetic isolation. Here, the reduced inter-grain connectivity performs a similar function, minimizing stray field (magnetostatic) and direct exchange interactions. Domain wall propagation through the structure is thus reduced, as is the energy penalty associated with anti-aligned grains that flip during the reversal process. In addition, the relatively smooth, regular grains free from asperities limit the nucleation of reverse domains as there is not the local focusing of demagnetization that occurs at corners. In contrast, a sample reduced for 24 hours (Fig. 2c) shows significant grain growth and increased connectivity. This leads to the loss of the regular structure that characterizes optimal samples, and results in a reduction in coercivity and squareness of the hysteresis loop (see Fig. 3c). Examining a sample cross section after partially completing the reduction process illuminates the role of porosity and calcium diffusion. After one hour at 875 °C SEM-EDS (Fig. 2d) demonstrates that Ca has fully penetrated only into the near-surface region, with a sharp boundary delineating its progress through the microstructure. Oxygen, samarium, and cobalt are distributed throughout the sample, as expected. Three distinct regions are formed: pristine Sm–Co–O in the center, a mixed region at the boundary of Ca penetration into the sample, and completely reduced SmCo<sub>5</sub>, near the surfaces of the sample. These correspond to three morphologically distinct regions, as shown in Fig. 2e–g. The near surface region forms the connected network of hexagonal SmCo<sub>5</sub> grains typical of high-coercivity samples, although the grain size is smaller than observed with longer holds, about 0.5 μm. The intermediate region is composed of finer smooth grains. Partially reduced particles in this region are likely composed of SmCoO<sub>3</sub>, Sm<sub>2</sub>O<sub>3</sub>, and Co, as cobalt is readily reduced in the presence of hydrogen between 500 and 800 °C.<sup>32</sup> Finally, the microstructure in the center of the sample resembles that of the precursor Sm–Co–O powder, structurally unchanged from its initial state.

The room-temperature magnetic properties of isotropic SmCo<sub>5</sub> produced *via*: drop casting particles on a graphite substrate; EPD; and molding all display coercivities >50 kOe (Fig. 3a). An impact of this extremely high coercivity is that an applied magnetic field of 140 kOe does not saturate the bulk samples. The random orientation of grains within the structure leads to a magnetic remanence,  $M_r \approx 5 \text{ kG}$  ( $= \frac{1}{2}M_s$ ),<sup>33,34</sup> as regions with easy axes at an angle to the external field relax to their equilibrium orientation. The fact that remanence exceeds 5 kG for the EPD sample suggests that the material is not entirely isotropic, as well as the presence of inter-grain interactions. Aligning and compacting these powders or inducing a preferential alignment during the AM process could enable formation of an anisotropic magnet, sharply increasing  $M_r$  while decreasing  $H_c$ . The extremely high coercivity makes this an attractive tradeoff and offers the potential for a high-performance high-temperature magnet. The high coercivity relative to the magnetization also makes the material resilient

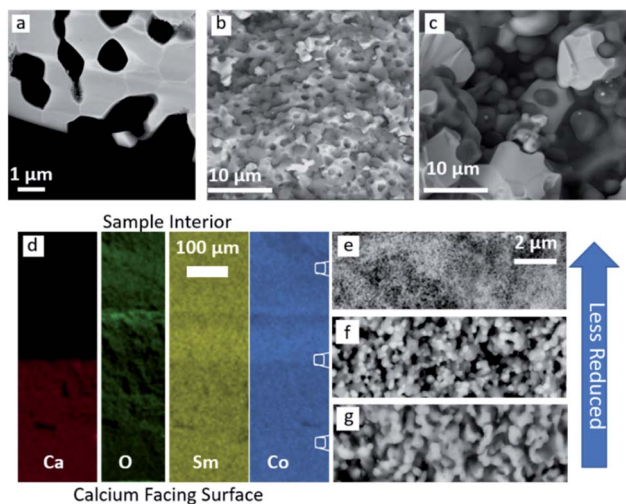


Fig. 2 Electron microscopy reveals a porous structure with micron-scale grains. (a) TEM images of single grains show sharp, regular grain boundaries and an open microstructure. SEM (b and c) images demonstrate the micron-sized hexagonal grains that lead to high coercivities (65 kOe, b) for samples reduced for 12 hours, contrasting the larger, irregular grains of a lower coercivity (40 kOe, c) sample reduced for 24 hours. Cross-sectional SEM-EDS images of a sample reduced for only 1 hour (d) reveal a reduction front that progresses across the sample, from the base (bottom of image) to the center (top of image), leading to the two-phase loop from Fig. 3e. Microscopy of grains in the un-reduced (e), transition (f), and fully reduced (g) regions reveal the grain growth process that accompanies the formation of highly coercive SmCo<sub>5</sub>.



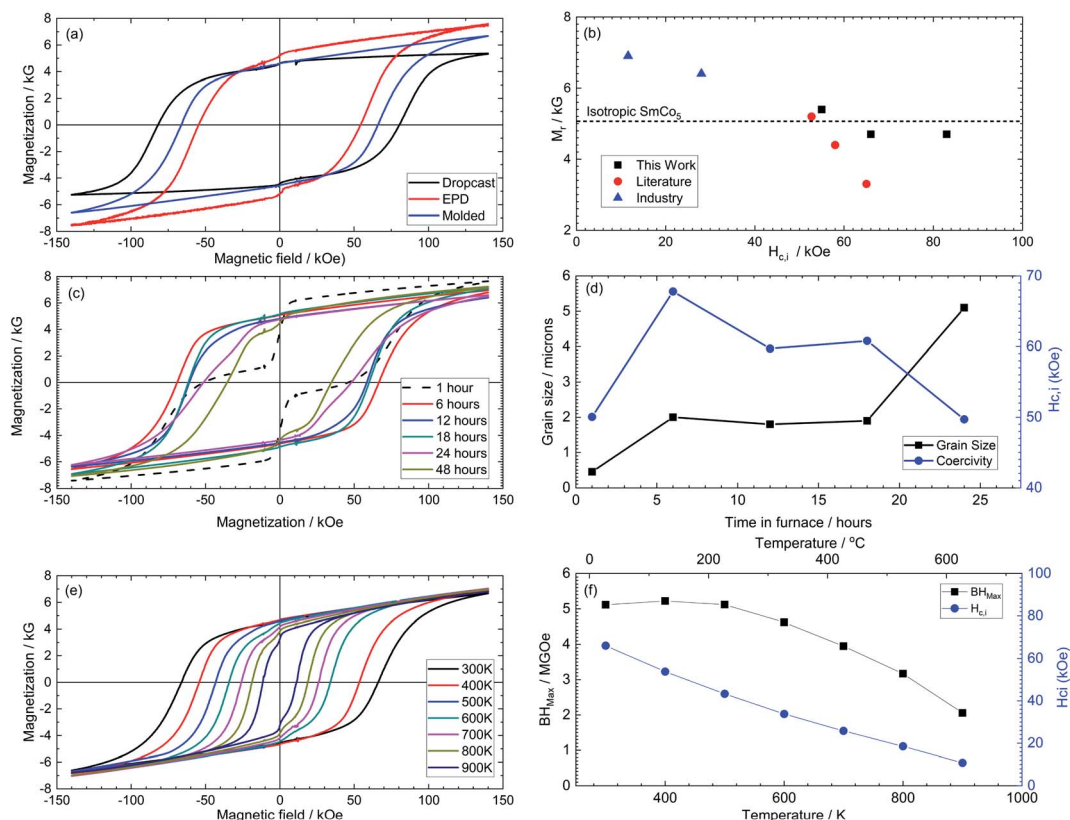


Fig. 3 Magnetic properties of Ca-vapor reduced SmCo<sub>5</sub> samples. (a) Room temperature  $M(H)$  loops for powder in distinct AM approaches. Increasing coercivity leads to a reduction in saturation and remnant magnetization. (b) The remnant magnetization and coercivity compared with reports from literature, and commercially available SmCo magnets. The coercivity of an ideal non-interacting isotropic SmCo<sub>5</sub> magnet is indicated by a dashed line. Sources for this data are discussed in the ESI Section 4.†. (c) Hysteresis loops at room temperature for bulk molded samples reacted at 875 °C for select dwell times. Short times result in not uniform reaction, while at long soak times there is significant grain ripening/growth leading to deteriorating magnetic properties. Coercivity extracted from this plot is presented in (d), along with long dimension of the oblate hexagonal grains, as determined by SEM, showing the window of time that leads to grains of ~2 microns, and thereby high coercivities. (e) Hysteresis loops for select temperatures for a molded sample showing excellent squareness. The energy products and coercivities are summarized in (f).

against self-demagnetization effects that could arise in ultra-thin or other extreme sample shapes.

Comparing the results of different techniques demonstrates that the percolation of Ca vapor through the Sm–Co–O powder during reduction determines final magnetic properties. Nanoparticles dispersed directly on a substrate yield the highest coercivity, greater than 80 kOe, and require only a one-hour hold at 875 °C. Conversely, direct mixing of oxide powder with calcium granules leads to much lower coercivity of 3 kOe (Fig. S3†) and is incompatible with reduction of bulk AM parts. Bulk samples (molded and EPD) require at least 6 hours to achieve complete, uniform reduction, and were typically soaked for 12 hours. The EPD sample (red curve Fig. 3a) shows some evidence of excess Co, revealed as a small step around zero field, likely due to pockets of oxide isolated from the Ca vapor such that only the cobalt is reduced. Nevertheless, excellent room temperature magnetic properties are achieved, for molded (66 kOe) and EPD parts (54 kOe), key parameters are summarized in Table 1. Note that decreasing coercivity correlates with increasing maximum magnetization, as the applied field is able to reverse more of the sample. The molded part compares

favorably with the best reports from other production methods including plasma spraying,<sup>35</sup> melt spinning,<sup>36</sup> and mechanical alloying.<sup>33,37</sup> Coercivity and remanence values are compared with literature and industry (data from Arnold Magnetic Technologies provides representative commercial values<sup>38</sup>) reports of isotropic Sm–Co in Fig. 3b,<sup>33,36,37</sup> a more detailed figure and references for the points therein is presented in Fig. S4 and table S1.† The extremely high coercivities are achieved without significant loss of magnetization relative to prior literature reports. Magnetization is reduced with respect to commercial SmCo magnets however, which are typically mixtures of SmCo<sub>5</sub> and Sm<sub>2</sub>Co<sub>17</sub>, as well as various additional alloying elements to enhance performance. The values reported for these samples are highly repeatable across the fabrication of more than 30 samples. Further, the vapor reduction technique is readily scalable – batches of samples can be reduced simultaneously – and portable: samples have been fabricated in several furnace configurations, using separate batches of oxide precursors.

Magnetic reversal in SmCo<sub>5</sub> typically proceeds *via* nucleation of reverse magnetic domains around localized areas of reduced anisotropy such as impurities or surface damage.<sup>19,20,39</sup> Once



**Table 1** Key magnetic properties of samples produced by drop-casting, molding, and electrophoretic deposition (EPD)

Sample type	Coercivity (kOe)	Remnant magnetization (kG)	Saturation magnetization (kG)
Dropcast	81	4.6	5.3
Molded	66	4.6	6.7
EPD	54	5.2	7.6

a region of anti-aligned magnetization is formed it can grow at the expense of neighboring regions through domain wall motion, eventually leading to reorientation of the whole sample. Nucleation can be suppressed by minimizing defects, surface damage, or sharp points which locally enhance the demagnetization field, while domain wall motion can be hindered by the controlled introduction of defects.<sup>21,40,41</sup> The tension between these two apparently contradicting requirements means there is no general solution to coercivity enhancement, rather material and microstructure-specific strategies must be employed. Reports of high coercivities have credited domain wall pinning on stacking faults,<sup>42</sup> Sm rich inclusions,<sup>42</sup> or grain boundaries.<sup>36,42</sup> Virgin magnetization curves for our samples (Fig. S1†) demonstrate that the limiting factor in magnetic reversal remains nucleation. There is at first a rapid increase in magnetization, followed by a more gradual increase above 10 kOe, indicative of nucleation followed by domain wall motion rather than pinning.<sup>21,40,41</sup> This suggests that the high coercivity originates in the high quality crystals and smooth surfaces which prevent local reductions in anisotropy field and increase in demagnetization at local chemical variations or sharp points, respectively. Thus, it is energetically unfavorable to nucleate a reverse domain, but comparatively easy for them to grow once they are formed. The disconnected nature of the grains (Fig. 2) further enhances coercivity by minimizing the energy penalty associated with an anti-aligned neighboring grain. Another factor that contributes to coercivity is grain size, with some work suggesting that the ideal grain for SmCo<sub>5</sub> is on the order of tens of nm,<sup>25,43</sup> with a Sm-rich composition.<sup>44</sup> However excellent coercivities are obtained here with much larger grains, on the order of 1.5 to 2 μm. Some evidence exists in the literature that larger grains can exhibit superior magnetic properties, for example Shen *et al.* found that 200 nm SmCo<sub>5</sub> NPs has a significantly larger coercive field than otherwise-identical 50 nm NPs.<sup>9</sup> Taking these factors together argues that the large coercivity arises from high quality SmCo<sub>5</sub> grains which are magnetically isolated from their neighbors (pores), and resist the formation of reversed magnetic domains due to their lack of defects minimizing local reductions in anisotropy fields and smooth surfaces minimizing locally enhanced demagnetization fields.

Additional insight into the magnetic properties may be gained by examining hysteresis and the grain structure of the samples at different stages of reduction with representative  $M(H)$  loops (Fig. 1c). Soaks under 6 hours resulted in an incomplete reduction process, leading to a two-phase loop

where SmCo<sub>5</sub> regions display a large coercivity, while Co + Sm<sub>2</sub>O<sub>3</sub> regions in the center of the sample remain magnetically softer. This leads to a reduction in the intrinsic coercivity, as approximately half of the sample moment reverses at low fields. The portion that has converted to SmCo<sub>5</sub> retains a high coercivity and is responsible for the portion of the loop that leads to a coercivity of 50 kOe. Square loops with high coercivities are obtained for samples soaked at 875 °C for between 6 and 18 hours, where the regular hexagonal grains of ~2 microns yield the highest coercivities, for reasons discussed above. Soaks of over 24 hours caused significant grain growth, increasing inter-grain connectivity, and leading to irregular shapes. The coercivity of these samples dropped commensurately as the larger grains with increased connectivity enhances propagation of reversed regions through domain wall motion and inter-domain interactions, and the irregular shapes reduced the energy barrier to the nucleation of reverse domains. It is notable that the mechanism for coercivity loss here is distinct from that in the case of 0.5 micron grains produced after a 1 hour soak. There the non-coercive portion of the sample leads to a reduction for VSM measurements that average across the entire sample volume, while here the coercivity is homogeneously reduced due to loss of the optimized grain structure.

The extremely high coercivity of the bulk SmCo<sub>5</sub> samples described here makes them ideal for high temperature applications (Fig. 3e and f). Coercivity declines as temperature increases as the greater thermal energy available makes it easier to rotate the magnetization. The coercive field exceeds 10 kOe at 600 °C, while the energy product decreases by only ~40% over the same range. Injection molded magnets typically suffer severe performance drops above 250 °C, showcasing the power of binder-free fabrication. Indeed, BHmax is effectively unchanged over the temperature range 0–200 °C, an operating window that encompasses most commercial motor and gearbox designs.  $M_r$  decreases as temperature increases towards the Curie point of SmCo<sub>5</sub>. Extrapolating the decrease in coercivity to higher temperatures suggests  $T_c \sim 730$  °C, which accords well with standard reports for SmCo<sub>5</sub> at ~750 °C.<sup>45</sup> The formation of a small low-field shoulder at elevated temperatures can be attributed in part to undesirable oxidation reactions in the measurement apparatus, wherein SmCo<sub>5</sub> decomposes into Sm<sub>2</sub>O<sub>3</sub> and Co, losing coercivity in the process. If coatings can mitigate this problem, it should be possible to achieve stable BHmax over a large temperature range, enabled by the excess coercivity. There is also a slight increase in  $M_s$  at elevated temperatures as the greater thermal energy available makes it easier to overcome magnetocrystalline anisotropy and align the magnetic moments with the external field. Calculating the reversible temperature coefficients for  $M_r$  and  $H_{c,i}$  across the full temperature range yields  $\alpha = 0.05\%/^{\circ}\text{C}$ , and  $\beta = 0.14\%/^{\circ}\text{C}$ .<sup>38</sup> These values are similar to results from literature or commercial SmCo magnets, but the significantly higher starting coercivity means that the maximum operating temperature for this material is much higher. Note that the value for  $\alpha$  must be treated with caution due to the reactions that are observed above 200 °C.



## Conclusions

A technique for producing phase-pure isotropic  $\text{SmCo}_5$  permanent magnets with extremely high coercivity has been developed, which is readily adapted to a range of advanced manufacturing techniques and provides a route towards net-shape fabrication of magnetic parts. A calcium vapor reduction process of  $\text{SmCoO}$  nanoparticles leads to the formation of extremely coercive  $\text{SmCo}_5$ , with bulk samples composed of randomly oriented, micron-sized, interconnected hexagonal particles. The production technique is simple and scalable and is intended to circumvent complex wet chemistry or environmental control requirements present in other demonstrations of extremely coercive  $\text{SmCo}_5$  particles. At room temperature, the coercivity of the material can exceed 80 kOe in powder form, or 66 kOe for a bulk piece, making the resulting magnets very resilient against demagnetization at elevated temperatures. The random orientation of the grains reduces  $M_r$ , necessitating future work either aligning powders during compaction, or the integration of an alignment mechanism such as an external field into the bulk fabrication processes demonstrated here. Achieving an anisotropic magnet while retaining this high coercivity will provide a new manufacturing route for  $\text{SmCo}$  magnets in demanding high temperature applications such as high temperature motors, magnetic couples, and non-contact bearings in extreme environments. This work represents an evolution in the practicality of the production of high-quality magnet powder, with a goal of producing a feedstock that is suitable for both traditional and advanced manufacturing techniques.

## Experimental section

### Materials

$\text{Sm}_x\text{Co}_y\text{O}_z$ , (nominally  $\text{SmCo}_5\text{O}_9$ ), nanoparticles were custom synthesized by Nanocerox (Ann Arbor, MI) using flame spray pyrolysis of controlled ratios of Sm and Co salts dissolved in organic solvents. Particle size was predominantly 20–50 nm, with some particles in the 50–100 nm range. Absolute ethanol was used as received; Tetraglyme; Ca granules, redistilled, 16 mesh, 99.5%; and 1 mm thick graphite electrodes were from Sigma-Aldrich; Alfa Aesar; and Ohio Carbon Blank; respectively. For characterization it was desirable to remove the calcium oxide from the sintered magnet. The calcium was removed from the monolithic sintered magnets by soaking them for 30 minutes in water saturated with bubbling argon gas.

### Nanoparticle deposition and reduction

Suspensions of nanoparticles were prepared by mixing the particles in absolute ethanol to a concentration between 1 and 2 volume% solids ( $\sim 50 \text{ mg ml}^{-1}$ ). A thin magnetic film can be prepared by drop-casting, or repeatedly dripping the solution onto the substrate and allowing the solvent to evaporate until the desired film thickness is reached. In general, better magnetic properties are obtained with thicker drop-cast layers. A typical sample mass per areal “surface density” for drop-cast

samples which led to sintered magnets with high coercivity was  $>20 \text{ mg cm}^{-2}$ . For thicker free-standing magnets suitable for near-net shape manufacturing we demonstrated three different techniques: Electrophoretic deposition (EPD), molding, and extrusion. The EPD setup consisted of two graphite electrodes inserted into a stirring ethanol bath of nanoparticles. A typical electric field of  $40 \text{ V cm}^{-1}$  resulted in a deposition of 2–4 millimeter-thick greenbodies on the cathode after minutes. To define the shape of the deposited magnet, the graphite was masked to block particle deposition using electrical tape. To avoid cracking of nanoparticle greenbody, a slow drying process was developed. After deposition samples were kept solvated by storing in a sealed container with excess solvent vapor (maintained using an absorbent wipe saturated with the solvent). A freeze dryer (Labconco FreeZone 4.5 liter,  $-105^\circ\text{C}$ ) was then used to lyophilize the samples. To freeze dry the samples were pre-frozen by placing them on a metal plate over an acetone-dry ice mixture ( $-77^\circ\text{C}$ ). Samples were placed in 50 ml pre-frozen glass drying chambers and lyophilized with a pressure of 0.01 mBar and temperature of  $-105^\circ\text{C}$  for 12–18 hours. For molding and extrusion techniques, a 14-volume percent suspension of  $\text{SmCo}_5\text{O}_9$  nanoparticles was mixed with Tetraglyme using a Flaktek centrifugal mixer at 3500 RPM for 5 minutes. The resulting shear-thinning paste was applied to silicone rubber molds using a spatula, or extruded from a syringe nozzle. After molding of the paste, the part was dried slowly to avoid cracking by covering with a glass Petri dish and maintained at  $90^\circ\text{C}$  for 3 to 5 days until drying was complete.

A single-step process was developed for sintering and reducing the deposited SmCo oxide materials while retaining their shape. Calcium granules were distributed in the bed of a stainless-steel boat, then covered by a stainless-steel screen to provide a gap between the sample and the molten calcium. The SmCo oxide greenbodies were loaded onto the screen and the boat was then covered loosely with a lid. Forming gas (4%  $\text{H}_2$  in Ar) was flowed over the sample, and the furnace was heated to a temperature above the melting temperature of calcium ( $842^\circ\text{C}$ ), typically  $875^\circ\text{C}$ . Hold times were varied between 1 hour and 48 hours after which the sample was extracted from the furnace while maintaining atmospheric control to quench the sample and retain the desired  $\text{SmCo}_5$  phase. This was achieved using a magnetically coupled push rod to move the sample out of the hot zone of the furnace without exposing the sample to atmosphere. A typical initial cooling rate over the first ten minutes was  $40^\circ\text{C}$  per minute.

### Measurements and microscopy

Measurements were performed using the vibrating sample magnetometer (VSM) option in a 16T Physical Properties Measurement System (Quantum Design). Samples were secured in gel-caps using non magnetic padding, or immobilized in the low-melting point PEG. For high temperature measurements the samples were tightly wrapped in oxygen-free copper foil and affixed to a resistive heater. Measurements were conducted in a high-vacuum environment to avoid undesirable sample oxidation. Grain structure was imaged using High-angle



annular dark-field scanning transmission electron microscopy (HAADF-STEM, FEI Titan 80-300) and scanning electron microscopy (SEM, FEI XL30S FEG). Composition maps were measured using energy-dispersive spectroscopy (EDS, EDAX Element detector, with TEAM software).

## Author contributions

Conceptualization: SEB, CAO, JDK, SKM. Data curation: SEB, AAB. Formal analysis: AAB, SKM. Funding acquisition: SKM. Investigation: SEB, AAB, CAO, MW, TL, ES, JD, JRIL. Methodology: SEB, CAO, JDK, SKM. Project administration: SKM. Resources: SEB, CAO, JDK, SKM. Supervision: SKM. Writing – original draft: SEB, AAB, SKM. Writing – review and editing: SEB, AAB, JRIL, SKM.

## Conflicts of interest

The authors declare no conflict of interest.

## Acknowledgements

This research was sponsored by the Critical Materials Institute, an Energy Innovation Hub funded by U.S. Department of Energy (DOE), Office of Energy Efficiency and Renewable Energy, Advanced Manufacturing Office. This work was performed under the auspices of LLNL under Contract DE-AC52-07NA27344.

## Notes and references

- 1 J. M. D. Coey, *J. Magn. Magn. Mater.*, 2002, **248**, 441–456.
- 2 H. Polinder, F. F. A. van der Pijl, G. de Vilder and P. J. Tavner, *IEEE Trans. Energy Convers.*, 2006, **21**, 725–733.
- 3 O. Gutfleisch, M. A. Willard, E. Brück, C. H. Chen, S. G. Sankar and J. P. Liu, *Adv. Mater.*, 2011, **23**, 821–842.
- 4 D. Brown, B.-M. Ma and Z. Chen, *J. Magn. Magn. Mater.*, 2002, **248**, 432–440.
- 5 V. Popov, A. Koptug, I. Radulov, F. Maccari and G. Muller, *Procedia Manuf.*, 2018, **21**, 100–108.
- 6 Y. Hou, Z. Xu, S. Peng, C. Rong, J. P. Liu and S. Sun, *Adv. Mater.*, 2007, **19**, 3349–3352.
- 7 Z. Ma, S. Yang, T. Zhang and C. Jiang, *Chem. Eng. J.*, 2016, **304**, 993–999.
- 8 Z. Ma, M. Yue, Q. Wu, C. Li and Y. Yu, *Nanoscale*, 2018, **10**, 10377–10382.
- 9 B. Shen, C. Yu, A. A. Baker, S. K. McCall, Y. Yu, D. Su, Z. Yin, H. Liu, J. Li and S. Sun, *Angew. Chem., Int. Ed. Engl.*, 2019, **58**, 602–606.
- 10 J. Ormerod, *Personal Communication, Magnet Applications*, 2019.
- 11 L. Li, A. Tirado, I. C. Nlebedim, O. Rios, B. Post, V. Kunc, R. R. Lowden, E. Lara-Curzio, R. Fredette, J. Ormerod, T. A. Lograsso and M. P. Paranthaman, *Sci. Rep.*, 2016, **6**, 36212.
- 12 C. Huber, C. Abert, F. Bruckner, M. Groenefeld, S. Schuschnigg, I. Teliban, C. Vogler, G. Wautischer, R. Windl and D. Suess, *Sci. Rep.*, 2017, **7**, 9419.
- 13 C. Huber, C. Abert, F. Bruckner, M. Groenefeld, O. Muthsam, S. Schuschnigg, K. Sirak, R. Thanhoffer, I. Teliban, C. Vogler, R. Windl and D. Suess, *Appl. Phys. Lett.*, 2016, **109**, 162401.
- 14 J. Jaćimović, F. Binda, L. G. Herrmann, F. Greuter, J. Genta, M. Calvo, T. Tomšič and R. A. Simon, *Adv. Eng. Mater.*, 2017, **19**, 1700098.
- 15 C. V. Mikler, V. Chaudhary, T. Borkar, V. Soni, D. Jaeger, X. Chen, R. Contieri, R. V. Ramanujan and R. Banerjee, *JOM*, 2017, **69**, 532–543.
- 16 N. Sridharan, E. Cakmak, F. A. List, H. Ucar, S. Constantinides, S. S. Babu, S. K. McCall and M. P. Paranthaman, *J. Mater. Sci.*, 2018, **53**, 8619–8626.
- 17 W. F. Li, T. Ohkubo and K. Hono, *Acta Mater.*, 2009, **57**, 1337–1346.
- 18 H. Sepehri-Amin, J. Thielsch, J. Fischbacher, T. Ohkubo, T. Schrefl, O. Gutfleisch and K. Hono, *Acta Mater.*, 2017, **126**, 1–10.
- 19 C. K. Mylvaganam and P. Gaunt, *Philos. Mag. B*, 1981, **44**, 581–593.
- 20 A. Verma, P. Verma and R. K. Sidhu, *Bull. Mater. Sci.*, 1996, **19**, 539–548.
- 21 A. Singh, V. Neu, S. Fähler, K. Nenkov, L. Schultz and B. Holzapfel, *Phys. Rev. B*, 2009, **79**, 214401.
- 22 M. Komuro, Y. Satsu and H. Suzuki, *IEEE Trans. Magn.*, 2010, **46**, 3831–3833.
- 23 B. Z. Cui, A. M. Gabay, W. F. Li, M. Marinescu, J. F. Liu and G. C. Hadjipanayis, *J. Appl. Phys.*, 2010, **107**, 09A721.
- 24 L. Zheng, B. Cui and G. C. Hadjipanayis, *Acta Mater.*, 2011, **59**, 6772–6782.
- 25 C. H. Chen, S. J. Knutson, Y. Shen, R. A. Wheeler, J. C. Horwath and P. N. Barnes, *Appl. Phys. Lett.*, 2011, **99**, 012504.
- 26 J. Nie, X. Han, J. Du, W. Xia, J. Zhang, Z. Guo, A. Yan, W. Li and J. Ping Liu, *J. Magn. Magn. Mater.*, 2013, **347**, 116–123.
- 27 D. Wang, X. Li, Y. Chang, M. Zhu, W. Li and M. Qi, *J. Rare Earths*, 2013, **31**, 366–369.
- 28 N. Poudyal and J. Ping Liu, *J. Phys. Appl. Phys.*, 2013, **46**, 043001.
- 29 L. Ye, K. Wen, Z. Zhang, F. Yang, Y. Liang, W. Lv, Y. Lin, J. Gu, J. H. Dickerson and W. He, *Adv. Energy Mater.*, 2016, **6**, 1502018.
- 30 B. H. Toby and R. B. Von Dreele, *J. Appl. Crystallogr.*, 2013, **46**, 544–549.
- 31 L. Liu, H. Sepehri-Amin, T. T. Sasaki, T. Ohkubo, M. Yano, N. Sakuma, A. Kato, T. Shoji and K. Hono, *AIP Adv.*, 2017, **8**, 056205.
- 32 H.-Y. Lin and Y.-W. Chen, *Mater. Chem. Phys.*, 2004, **85**, 171–175.
- 33 Y. Liu, M. P. Dallimore, P. G. McCormick and T. Alonso, *J. Magn. Magn. Mater.*, 1992, **116**, L320–L324.
- 34 J. Wecker, M. Katter and L. Schultz, *J. Appl. Phys.*, 1991, **69**, 6058–6060.
- 35 K. Kumar, D. Das and E. Wettstein, *J. Appl. Phys.*, 1978, **49**, 2052–2054.





- 36 S. Koppoju, V. Chandrasekaran and R. Gopalan, *AIP Adv.*, 2015, **5**, 077118.
- 37 J. Ding, P. A. I. Smith, P. G. McCormick and R. Street, *J. Magn. Magn. Mater.*, 1996, **161**, 303–308.
- 38 Samarium Cobalt Magnets, <https://www.arnoldmagnetics.com/products/recoma-samarium-cobalt-magnets/>, accessed 18 January 2022.
- 39 K. Bachmann, *IEEE Trans. Magn.*, 1971, **7**, 647–650.
- 40 J. M. D. Coey, *Magn. Magn. Mater.*, 2010, 253.
- 41 Y. K. Takahashi, T. O. Seki, K. Hono, T. Shima and K. Takanashi, *J. Appl. Phys.*, 2004, **96**, 475–481.
- 42 O. Akdogan, H. Sepehri-Amin, N. M. Dempsey, T. Ohkubo, K. Hono, O. Gutfleisch, T. Schrefl and D. Givord, *Adv. Electron. Mater.*, 2015, **1**, 1500009.
- 43 O. Akdogan and N. M. Dempsey, *J. Appl. Phys.*, 2014, **115**, 17E508.
- 44 J. Ding, P. G. McCormick and R. Street, *J. Alloys Compd.*, 1993, **191**, 197–201.
- 45 W. E. Wallace, *Rare Earth Intermetallics*, Elsevier, 1973.

